Photovoltaic Failure Detection Based on String-Inverter Voltage and Current Signals

MARCO-ANTONIO ZUÑIGA-REYES[1,2]**, (Member, IEEE), JOSE-BILLERMAN ROBLES-OCAMPO**[3]**,**
PERLA-YAZMÍN SEVILLA-CAMACHO[3,4]**,**
JUVENAL RODRÍGUEZ-RESÉNDIZ[5]**, (Senior Member, IEEE),**
ORLANDO LASTRES-DANGUILLECOURT[1]**,**
AND JORGE-EVARISTO CONDE-DÍAZ[1,6]**, (Member, IEEE)**

[1]Institute for Research and Innovation in Renewable Energies, Universidad de Ciencias y Artes del Estado de Chiapas, Tuxtla Gutiérrez 29039, Mexico
[2]Electric and Electronic Engineering Department, Tecnológico Nacional de México en Tuxtla Gutiérrez, Tuxtla Gutiérrez 29050, Mexico
[3]Energy and Sustainability Academic Group, Universidad Politécnica de Chiapas, Suchiapa 29150, Mexico
[4]Academic Program of Mechatronic Engineering, Universidad Politécnica de Chiapas, Suchiapa 29150, Mexico
[5]Faculty of Engineering, Universidad Autónoma de Querétaro, Santiago de Querétaro 76010, Mexico
[6]CONACyT, Institute for Research and Innovation in Renewable Energies, Universidad de Ciencias y Artes del Estado de Chiapas, Tuxtla Gutiérrez 29039, Mexico

Corresponding author: Perla-Yazmín Sevilla-Camacho (psevilla@upchiapas.edu.mx)

ABSTRACT The existence of failures in photovoltaic systems causes energy losses, security problems, and damage to its components. Therefore, it is necessary to develop monitoring systems to improve their productivity, reliability, efficiency, and safety. This work proposes a method for detecting and indicating short-circuit failure and partial shading present in grid-connected photovoltaic modules. The novelty of this proposal is the processing of voltage and current signals generated (ripple signals) by the electrical interaction between the photovoltaic string, the photovoltaic inverter, the condition of the modules, temperature, and irradiance. The magnitudes of specific frequency components are obtained from these electrical signals using DFT, and Cartesian coordinates are formed in a three-dimensional plane. Coordinates belonging to each of the string conditions are mostly located in different octants from this plane. This distribution allows an assessment of the modules state. Certain scattering is solved with a K-nearest neighbors algorithm. The effectiveness of the methodology was experimentally validated in two PVG with different characteristics. In each test case, the method was adaptable to the real conditions of the photovoltaic system. The results show effectiveness greater than 90% in the first evaluation levels, there is a slightly lower detection certainty in anomalous conditions with coordinates that are very close to each other. However, the system has 100% certainty detecting the presence of an abnormal condition. The method allows adaptation to different conditions, and takes advantage of the electrical signals derived from the actual performance of the used devices.

INDEX TERMS Fault detection, frequency components, grid-connected system, photovoltaic inverter, photovoltaic module.

NOMENCLATURE

$\propto$	Negative voltage factor due to temperature
a_0	0 Hz component
a_{2fg}	$2f_g$ Hz component
$arrC$	String condition state
d	Euclidean distance
dbV	Database
dbV'	Normalized database
dV	Distance vector
evV	Evaluation vector
evV'	Normalized evaluation vector
f_g	Grid frequency
G	Irradiance
I	Current
I_g	Grid current

V_{mp}	Maximum-power point voltage
I_m	Maximum current
i_{ripple}	Ripple current
I_{scs}	Short-circuit string current
I_{sc}	Short-circuit current
i_{str}	String current
K_{PV}	Utilization ratio
n_d	Number of diodes activated due to partial shadow
P	Power
P_m	Maximum power
T	Temperature
V	Voltage
V_g	Grid voltage
V_{hf}	High-frequency voltage
V_{lf}	Low-frequency voltage
I_{mp}	Maximum-power point current
V_m	Maximum voltage
V_{ocs}	Open-circuit string voltage
V_{oc}	Open-circuit voltage
v_{ripple}	Ripple voltage
v_{str}	String voltage
AC	Altern current
AI	Artificial intelligence
DC	Direct current
DFT	Discrete Fourier transform
DWT	Discrete wavelet transform
KNN	K-nearest neighbors algorithm
MPPT	Maximum power point tracker
PS	Partial shading
PVA	Photovoltaic array
PVG	Photovoltaic generator
PVI	Photovoltaic inverter
PVM	Photovoltaic module
PVS	Photovoltaic string
SC	Short circuit

I. INTRODUCTION

The rapid growth of electricity generation through photovoltaic technology has allowed photovoltaic installations to generate and consume electricity [1], which electrify urban regions more easily. However, photovoltaic systems are subjected to adverse conditions, both environmental and physical, which cause a decrease in the electrical energy generated. For example, when there is a non-uniform distribution of irradiance (G), a partial shading condition (PS) is caused. This condition of the photovoltaic generator (PVG) is considered transient and easily located through visual inspection. On the other hand, a short circuit (SC) is regarded as an abnormal condition due to a physical cause. The SC causes a constant decrease in power and is difficult to identify by visual inspection. Therefore, various methodologies have been developed to determine the condition of a PVG. The methodologies take many features into accounts, such as the electrical characteristics of the photovoltaic modules (PVMs), the electrical configuration chosen for their connection, and some variables.

These variables are temperature (T), irradiance, current (I), voltage (V), and power (P).

The methods reported for determining the condition of photovoltaic generators (PVGs) are classified into three categories: 1) use of instantaneous values of electrical parameters, 2) analysis of the $I - V$ and $P - V$ curve, and 3) use of unconventional parameters. In the first category, the determination of the state of the PVG is based on the comparison of the instantaneous values of I and V. These signals are obtained from experimental and simulated tests carried out under specific conditions of G and T. This technique is applied in [2] to determine the presence of short-circuit modules and open-circuit modules on a PVG. The PVG is made up of various photovoltaic strings (PVSs), whereby each PVS is connected to a MPPT [3]. A similar proposal is presented in [4], where the open-circuit conditions in a PVS, general shading, and partial shading in sections of a PVM were determined. The analysis of the condition of the photovoltaic system was based on an Elman-type neural network. In this detection category, the simulation of the PVG, carried out under various conditions, causes an increase in the devices that are needed for determining the PVG state. Furthermore, some methodologies require the calculation of intermediate parameters that require specific processing, which causes an increase in the requirements in general.

In the second detection category, $I - V$ and $P - V$ curves are used to determine the PVG conditions. These curves allow a representation of the simulated or experimental response of the set of PVMs that are in the direct current (DC) section of a PVG. Both curves have a specific shape when it belongs to a PVG in healthy state. However, these curves show significant changes when abnormal conditions affect the PVG. The variation was used to indicate the presence of failures in the PVG. Pattern recognition and normalized curves were used for this purpose [5].

On the other hand, the $I - V$ curve was analyzed to obtain specific parameters, such as open-circuit voltage (V_{oc}), short-circuit current (I_{sc}), maximum voltage (V_m), and maximum current (I_m) [6]. The analysis determines the conditions of short circuit, open circuit, aging, and partial shading. Discrete wavelet transform (DWT) is applied to the $I - V$ curve to determine the presence of partial shading in a PVS [7]. The determination was possible because the DWT coefficients presented a specific behavior for each analyzed condition. Alternatively, the $P - V$ curve is used to detect different partial shading conditions in a photovoltaic array (PVA) [8]. The determination was performed to relocate the PVM in case of failures detection. All the second detection category methodologies have a drawback: disconnecting the PVMs segment to be analyzed, thus resulting in zero energy production [6], [8]–[10].

The third detection category corresponds to methodologies using non-conventional parameters. The capacitance to ground and reflectometry techniques were used in [11] to determine the state of a PVA. The identified conditions are PVM disconnection and PVM degradation.

On the other hand, statistical techniques were used to determine the location of the PVS in failure condition [12]. The state of each PVS was determined using only the magnitude of the normalized current. Another methodology of the third category is presented in [13]. The methodology identifies the PVSs with open-circuit failure. The identification was possible by analyzing the frequency response of the set of PVMs. These tests were carried out under conditions of zero irradiance, and one of the PVMs was struck by a pulsing light at a specific frequency (f_{ind}). Therefore, the open-circuit location in the PVS was determined by a variation in the magnitude of the induced frequency component.

Another methodology to determine the PVM conditions is proposed in [14]. Open-circuit and partial shading conditions are determined unlike the previously commented research. The equations that describe the electrical and thermal behavior of a PVM were used. A thermographic camera was used to validate the proposed method. The validation implied special equipment and qualified personnel to perform the measurements. All the methodologies presented in this category require specific conditions or equipment for their application, increasing the total costs of the system.

In a device with an integrated MPPT, the voltage of the PVM assembly presents oscillations resulting from the execution of the algorithm programmed in the MPPT [15]. The oscillations present variations in the magnitude and shape of the voltage and current signals, which are called the ripple voltage and ripple current [16]. These signals contain information that is representative of the condition of the PVS. Therefore, this work proposes a method for determining failures in a PVS by using the v_{ripple} and i_{ripple} signals generated from the interaction between the PVS and the PVI. The proposed method uses the Discrete Fourier transform and the K-nearest neighbors algorithm. DFT is a technique used to extract the characteristics of signals in the frequency domain, whereas KNN is a learning technique that belongs to artificial intelligence. KNN works for both supervised and unsupervised learning, and its main characteristic is taking into consideration all the training data. KNN is applied to solve classification and regression problems because of its simplicity of operation.

The proposed method allows the detection of short-circuit conditions and partial shading on the PVMs. The detection based on the PVG signals allows the use of a minimum number of elements, mainly those necessary to carry out the data acquisition. Also, the system operates online and in real-time. Compared to other reported works, none of them take advantage of the interaction between PVS and PVI. Ripple voltage and ripple current have not been used to indicate the condition of a grid-connected photovoltaic system. In addition, the proposed system performs a greater sampling of the variables to better represent the phenomenon. Easy to acquire sensors and measuring devices are used for this purpose.

Furthermore, the methodology proposed in this article does not require the execution of simulations, which allows its implementation in low computing power equipment. The use
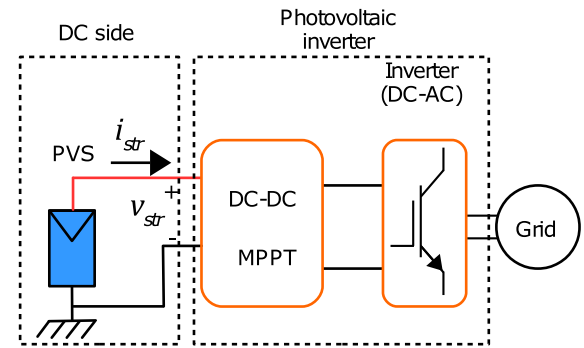

FIGURE 1. General diagram of an electrical grid-connected PVG.

of the KNN method allows a learning whose training time is short. Finally, this proposal does not require the disconnection of the analyzed PVS, which guarantees a performance free of interference to the PVG.

The rest of the article is organized in the following manner. Firstly, Section II presents the theoretical background needed to understand the ripple voltage and the variation it undergoes due to the operating conditions of a PVS. Secondly, Section III describes the proposed failure detection method. The simulation of a grid-connected PVG is carried out in Section IV. Next, Section V presents the experimental setup and the presentation of interest cases, while results are analyzed in Section VI. A discussion section is presented in VII. Finally, the conclusions of this study are presented in Section VIII.

II. THEORETICAL BACKGROUND

A grid-connected PVG is a set of electronic components working in a coordinated way to send energy to the electrical grid [17], [18]. The process begins with PVMs that convert the energy from sunlight to useful electrical energy. However, the DC voltage delivered by the PVMs is not compatible with the grid. The incompatibility is solved by the PVI, which takes a voltage signal in DC and converts it to voltage in alternating current (AC) with adequate amplitude (V_g) and frequency of the electrical grid (f_g). Both V_g and f_g must meet the standards of the electrical grid to which the PVG is connected [18]–[20].

Figure 1 shows the two main sections of a PVI. The first section is the DC to DC voltage converter [21], which maintains the fixed voltage that will serve as the basis for AC investment. This section implements the MPPT algorithm, which continuously searches for a combination of V and I that provide the highest electrical power to the grid. The second section of the inverter corresponds to the process of converting DC voltage to AC voltage. The output stage of this section makes the coupling to the electrical grid. This coupling must guarantee an interference-free connection, and the generated signal will induce a minimum number of harmonics to the line to which it is being coupled. The $DC-AC$ convertion method will depend on the PVI designer. The aforementioned does not allow a general characterization of all converters of this type [20].
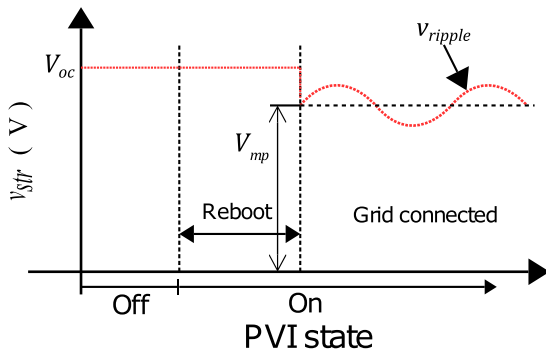
FIGURE 2. Variation of the v_{str} waveform as a function of the PVI status.

FIGURE 3. Location of the maximum power point under different conditions of the PVS.

On the other hand, Fig. 2 shows that a PVI simultaneously operates in two stages. During the initial start-up stage, the input voltage to the PVI corresponds only to the open-circuit voltage (V_{oc}) delivered by the PVA. Then, the PVI goes into synchronous with the grid, and the V_{ripple} is generated [22]. Therefore, the voltage signal comprises three components in the inverter input section. The signals comprise a signal with constant displacement, a low-frequency signal, and a high-frequency signal. The high-frequency signal is typical of the $DC-AC$ voltage convertion process. The inversion frequency is selected by the PVI designer and set between 10 kHz and 50 kHz [23], [24]. Equation 1 represents the input voltage to the PVI (v_{str}). The signal only exists when the inverter interacts with the PVMs set.

$$v_{str} = V_{mp} + V_{lf} + V_{hf} \qquad (1)$$

It is essential to mention that V_{mp} is variable and depends on the PVS condition. Low and high-frequency components shall be visible when the sampling frequency is equal to or greater than twice the V_{hf} frequency value. A sampling frequency with this feature fulfills the Nyquist theorem.

The magnitude of V_{mp} in a PVS in a healthy state (Hty) is variable due to irradiance and temperature [16]. However, the value of V_{mp} changes significantly when abnormal operating conditions occur. The variation of V_{mp} causes small changes in V_{lf} and V_{hf}, and these changes are difficult to detect in the time domain. Therefore, there are two conditions to consider in the ripple voltage analysis. First, the variation of V_{mp} under different environmental and physical conditions must be understood. Second, the analysis of the ripple signal is found in the frequency domain.

A. MAXIMUM POWER VOLTAGE

The maximum power value (P_m) is located at the point at which the product is the global maximum on the $I-V$ curve, obtained from Eq. (2).

$$P_m = max(V_x I_x) \qquad (2)$$

where x is the position of the data vectors of V and I. The MPPT algorithm locates the position of maximum power for a PVI, and causes variations in both V_{mp} and I_{mp}. The variations are in agreement with the conditions of the PVS. Therefore,
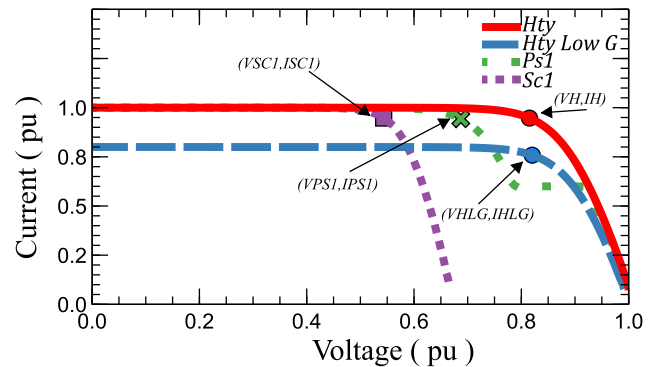
it is appropriate to back up variations of V_{mp} and I_{mp} with the $I-V$ curve.

The theoretical analysis of the $I-V$ curve of a PVS requires taking into account multiple parameters, irradiance, temperature, quantity (n) of PVMs, and the data provided by the datasheet. Therefore, if a PVS is composed of n PVMs, then the PVS open-circuit voltage (V_{ocs}) is obtained by Eq. (3). Moreover, the maximum current obtained from a PVM is I_{sc}. The short-circuit current of a PVS (I_{scs}) is obtained by Eq. (4).

$$V_{ocs} = n(V_{oc} + \propto (T - 25)) \qquad (3)$$

$$I_{scs} = \frac{I_{sc}G}{1000} \qquad (4)$$

The ordered pairs (V_x, I_x) of the $I-V$ curve are obtained by calculating the current (I_x) that satisfies a specific condition of V_x, considering that V_x varies from 0 to V_{ocs}. Figure 3 shows normalized I-V curves for different PVS conditions. The first analysis considers the PVS in two health conditions, albeit with different irradiance levels. The first healthy condition, named Hty, is obtained with a G of 1000 Wm^{-2}. The second healthy condition is named $HtyLowG$, which is obtained from a G of 800 Wm^{-2}. Figure 3 shows that both curves are similar, but the $HtyLowG$ curve presents a lower current generation due to the lower irradiance level. The maximum power points for Hty and $HtyLowG$ are found at the Cartesian coordinates (VH, IH) and ($VHLG$, $IHLG$), respectively. Figure 3 also show that the VH and $VHLG$ components are very close. However, IH and $IHLG$ take quite different values.

On the other hand, Fig. 3 shows that the $I-V$ curve acquires a different shape when the condition of partial shading, named $PS1$, exists. It compared to the $I-V$ curve in the healthy state. This variation is directly related to the shading area and the number of protection diodes that the PVMs have. The internal structure of a PVM is analyzed below to better understand this phenomenon. Figure 4(a) shows that a PVM consists of s sections of photovoltaic cells (PVCs), and each section is protected by a diode in reverse bias, see Fig. 4(b). The protection diodes come into operation when the cells to protect are uncoupled [7], [14]. Each uncoupled segment
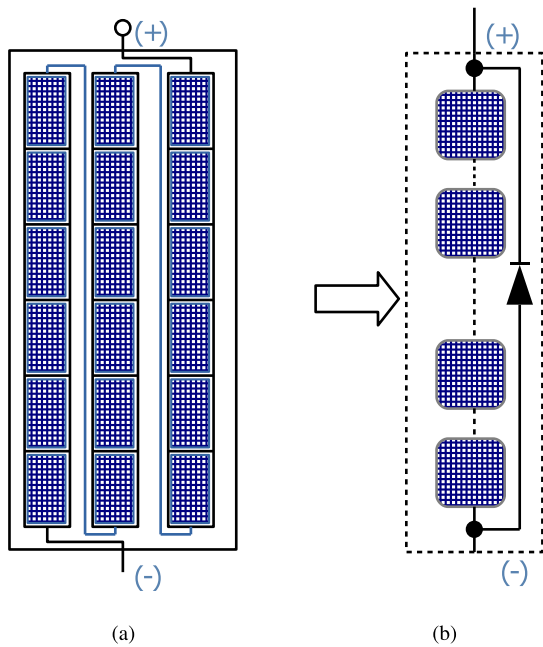
(a)   (b)

FIGURE 4. The architecture of a PVM. (a) Module composed of 3 cell segments, and (b) Cell segment protected by a diode.

causes a voltage loss (V_{oc}/s). Therefore, the magnitude of the voltage corresponding to the maximum-power point for the partial shading condition (*VPS1*) can be obtained with Eq. (5), using the value of the *VH* component present in the *Hty* condition as reference.

$$VPS1 = VH - \frac{n_d}{s} V_{oc} \qquad (5)$$

The partial shading condition analysis concludes with the *PS1* curve of Fig. 3. This curve presents a P_m located at the Cartesian coordinates (*VPS1*, *IPS1*) and has a significant change between the value of *VPS1* and *VH* components. However, the value between the *IPS1* and *IH* components varies very little. Therefore, the variable V_{mp} takes the value of the *VPS1* component for the partial shading condition.

On the other hand, Fig. 3 shows the $I - V$ curve obtained when the short-circuit condition, named *SC1*, occurs in a PVS. This curve also takes a different shape compared to the conditions mentioned above. The *SC1* condition can be observed when a PVM does not provide power to the string where it is connected. In addition, there are 0 V between terminals. Figure 3 shows that the presence of the short circuit causes a significant displacement of the position at the maximum-power point. This displacement places the point of maximum power in the Cartesian coordinates (*VSC1*, *ISC1*). The *ISC1* component will have the same magnitude as the current obtained in the *PS1* condition, while the value of the *VSC1* component for *m* modules in a short circuit is obtained through Eq. (6). Consequently, V_{mp} will be equal to the *VSC1* component.
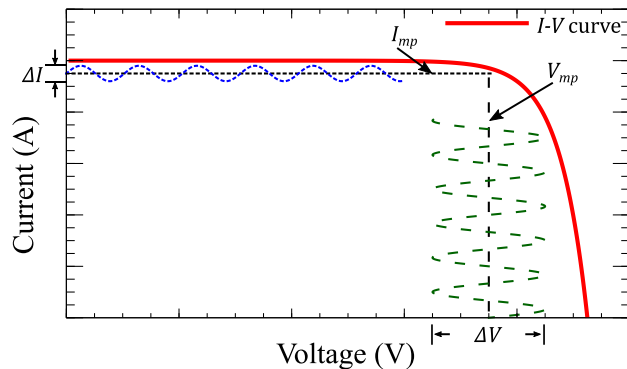
$$VSC1 = VH - mV_{oc} \qquad (6)$$

FIGURE 5. Variation effect of I_{mp} on V_{mp}.

B. RIPPLE VOLTAGE
The $I - V$ curve is a convenient way of analyzing the static behavior of the PVS. However, when PVI is operating, both I_{mp} and V_{mp} oscillate at a specific frequency [22]. In [20], [24] is shown that this frequency corresponds to $2f_g$, and its amplitude depends on the magnitude of ΔI. Figure 5 shows the relationship between ΔV and ΔI.

The maximum value of ΔV is obtained by means of Eq. 7.

$$\Delta V = \sqrt{\frac{2(K_{PV} - 1)P_m}{3\eta V_{mp} + \beta}} \qquad (7)$$

ΔV will be determined by V_{mp} and P_m when K_{PV}, η, and β have constant values. Therefore, for each condition presented in Figure 3, ΔV will be different. In some cases, these changes are small; however, the PVI responds to these changes based on its control system. Consequently, for two different PVI, the waveform of both signals will have different frequency components. A more detailed analysis of the v_{ripple} calculation can be found in [3].

III. FAILURE DETECTION METHOD
The proposed method includes a training stage and a detection or decision-making stage. Figure 6 shows the flowchart of the proposed method, which is divided into four processes. In *Process 1*, the data acquisition is performed, and the DFT is applied. The storage and normalization of the data acquired and digitally processed during *Process 1* are carried out in *Process 2*. Next, *Process 3* involves the training of the KNN network. Once the training is done, *Process 4* is carried out; a data vector is introduced at the input of the KNN network. The category to which the vector of entry belongs is obtained using the KNN algorithms.

A. PROCESS 1
The first step is acquiring the T, G, v_{str}, and i_{str} signals that the PVS generates under three conditions: healthy, partial shading, and short circuit. The acquisition is performed at fixed sampling frequency f_s, and Z sampling are acquired from each condition. p samples are acquired for each sampling. After the acquisition, the absolute value of the frequency components of the v_{str} and i_{str} signals is obtained.
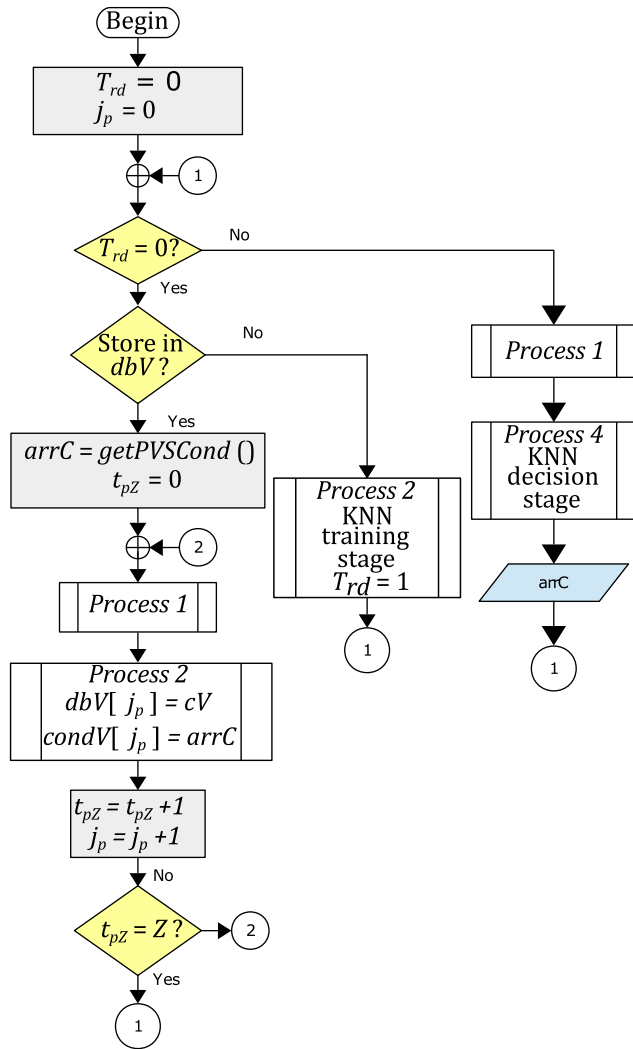
FIGURE 6. Flowchart of the proposed method. In the first stage of the process the database is obtained. The training takes place in the next stage. Finally, decision-making is repeated indefinitely.

The DFT definition is used for that, along with Eq. (8) and Eq. (9).

$$V_F = \left| \sum_{\partial=0}^{p-1} v_{str}(\partial) e^{-j\frac{2\pi}{p}F\partial} \right| \rightarrow F = 0, 1, \ldots, p-1 \quad (8)$$

$$I_F = \left| \sum_{\partial=0}^{p-1} i_{str}(\partial) e^{-j\frac{2\pi}{p}F\partial} \right| \rightarrow F = 0, 1, \ldots, p-1 \quad (9)$$

where V_F and I_F are the vectors that contain the absolute magnitudes of the frequency components. The T signal, G signal and obtained data are stored in the vector of magnitudes of frequencies of interest, called cV, which has the structure shown in Eq. (10). The detailed description of all of *Process 1* is shown in the flowchart of Fig. 7.

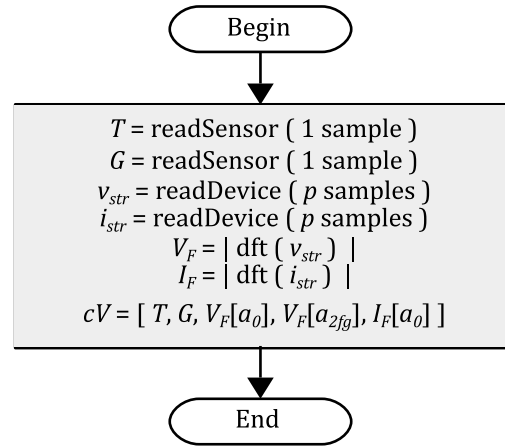$$cV = [T, G, V_F(a_0), V_F(a_{2fg}), I_F(a_0)] \quad (10)$$

FIGURE 7. Flowchart used to obtain the *cV* vector of each condition of the PVS.

B. PROCESS 2

This process is part of the training stage, and it creates an array called $dbV[j_p]$ with $j_p = 1, 2, \ldots, h$, where h represents the maximum record number. This matrix stores the cV vectors that were obtained in *Process 2* (see, Eq. (11)). These vectors are the records that identify the behavior of a PVG and which will be used in *Process 3*. On the other hand, the detected condition of the PVS is assigned by integer values stored in a variable called $arrC$ with $arrC = 1, 2, \ldots, c$, where c is the maximum value of possible conditions. All the PVS conditions are stored in a vector called $condV[j_p]$ with $j_p = 1, 2, \ldots, h$, where h is the maximum record number. The vector is obtaining with Eq. (12). *Process 2* is cyclical, and its duration will be determined by the conditions imposed in Fig. 6.

$$dbV[j_p] = cV \quad (11)$$
$$condV[j_p] = arrC \quad (12)$$

C. PROCESS 3

This process is also part of the training stage and consists of applying the KNN algorithm to perform supervised learning [10], [25]. The KNN requires two input elements for this purpose [26], [27]. Figure 8 shows that the first element is the $condV[j_p]$ vector, and the second element is the $dbV'[j_p]$ matrix. The matrix contains the normalized elements of the $dbV[j_p]$ matrix, which was stored during *Process 2*. Normalization is a requirement of the KNN technique, and this is carried out in the training and decision-making stages. This normalization allows obtaining input values less than or equal to one, regardless of the difference in orders of magnitude between the variables.

The normalization of the training stage data consists of multiplying the elements of the register stored in $dbV[j_p]$ with a vector named $K_n[b]$, where $b = 1, 2, \ldots, 5$. The value of each of the elements of $K_n[b]$ is obtained using the procedure indicated in Fig. 9, which is called the normalization initiation stage in Fig. 8. T has the value of 25 °C,
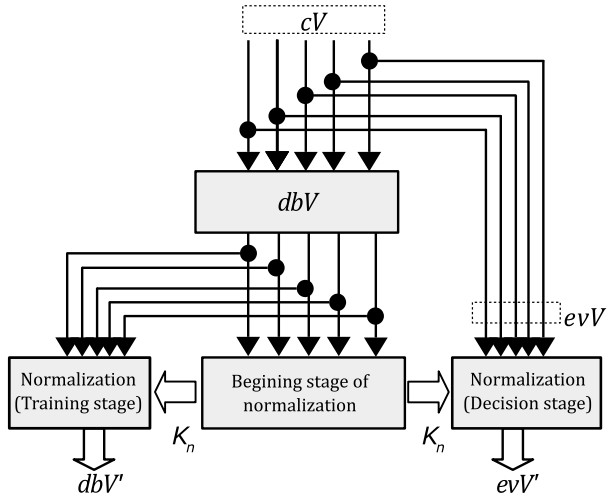
FIGURE 8. Graphic representation of the normalization process used in the training and decision stages.
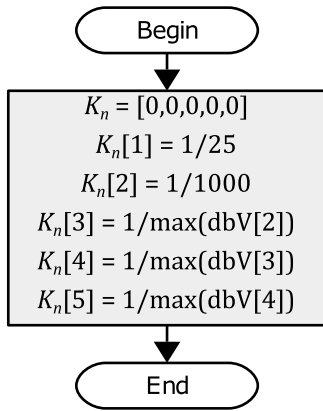

FIGURE 9. Initialization stage of normalization.

which is the theoretical reference temperature to generate a voltage variation of the PVM due to temperature, whereas G has the value $1000\,\mathrm{Wm}^{-2}$, which is the maximum irradiance considered theoretically for a PVM.

The $dbV'[j_p]$ matrix can be obtained through the procedure described in Fig. 10. The procedure is carried out once the $K_n[b]$ vector is acquired. The KNN training function proposed by the Python Scikit library is used once the normalization of dbV vector is carried out. KNN only organizes training data in quick access structures such as Ball Tree or KD Tree, unlike other artificial intelligence techniques. The value of 1 is assigned to the variable T_{rd} to indicate the end of the KNN training.

D. PROCESS 4

The classification of a particular case is carried out after *Process 3*. This process is also called the decision-making stage. A vector, called evV', is introduced to the decision-making. The vector contains the normalized elements of the evV vector (see Fig. 8). This last vector contains five elements with structure and variables identical to the vector cV (see Eq. (10)), which were acquired in *Process 1*. The
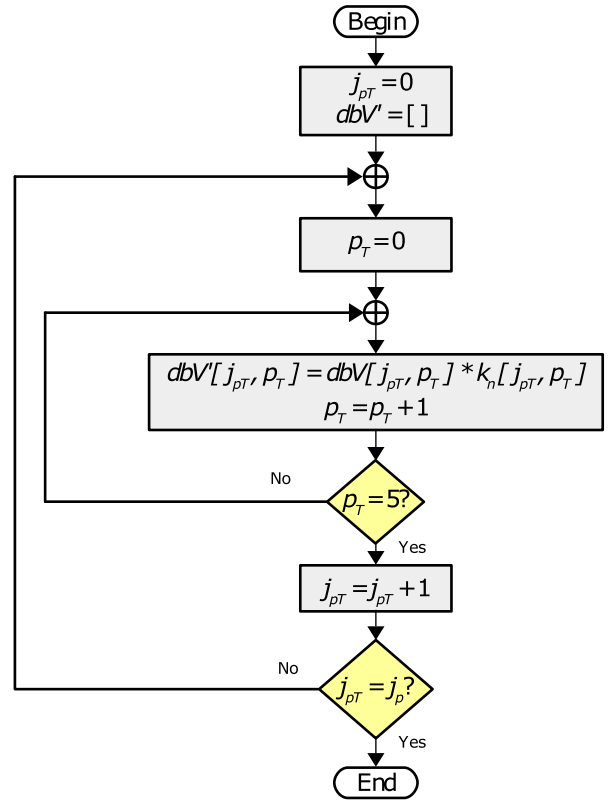

FIGURE 10. Procedure to obtain the $dbV'[j_p]$ matrix.

data are not stored but are normalized after its acquisition, unlike the training stage. The normalization process is the same as that applied to the training stage during *Process 3* (Figures 9 and 10). A mathematical algorithm is used to locate the KNN within the $dbV'[j_p]$ matrix, considering the input vector evV' origin. This procedure is carried out once the normalized input vector evV' has been obtained.

The most widely used mathematical procedure is that of the Euclidean distance, the definition of which is shown in Eq. (13).

$$d(evV', dbV') = \sqrt{\sum_{i=1}^{5}(evV'_i - dbV'_i)^2} \qquad (13)$$

where $i = 1, 2, \ldots, 5$, which is the maximum value of parameters that each one of the analyzed vectors contains.

A vector of distances, called $dV(d, arrC)$, is formed after obtaining the Euclidean distances. The vector is composed of j pairs, ordered from least to most significant as d distance function (see Eq. (14)). The number of times each category appears in the $dV(d, arrC)$ vector is counted because $arrC$ may take the value of one or more categories or conditions of the PVS. Finally, the test vector is assigned the category with the highest number of matches in the $dV(d, arrC)$ vector.

$$dV(d, arrC) = [[d_0, arrC_0],$$
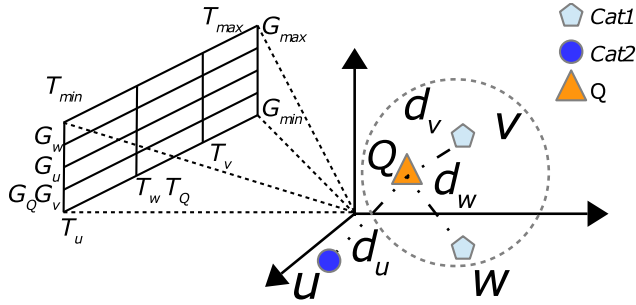$$[d_1, arrC_1], \ldots, [d_{j-1}, arrC_{j-1}]] \qquad (14)$$

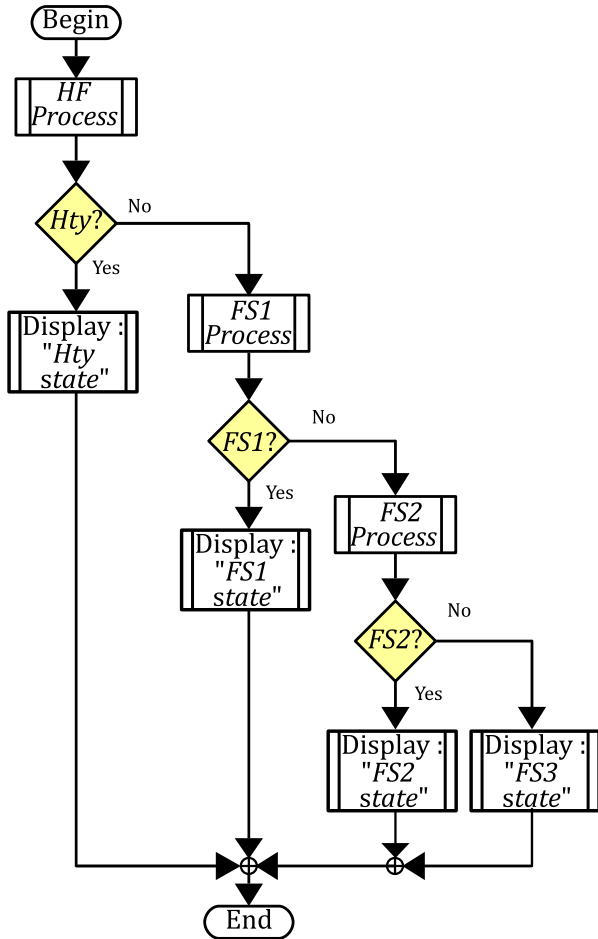**FIGURE 11.** Graphical representation of the Euclidean distance.

FIGURE 12. Flowchart for the general decision-making sequence.

TABLE 1. Simulated tests.

G (W/m^2)	Condition	Id
1000	Hty	$HtyG1000$
1000	$Sc1$	$Sc1G1000$
1000	$Ps1$	$Ps1G1000$
500	Hty	$HtyG500$

TABLE 2. Characteristics of the simulated modules.

Id	Description	Characteristics
PVM	Photovoltaic module SHARP, model NU_S5_E3E	48 solar cells
		V_{oc}= 30.2 V
		I_{sc}= 8.54 A
		V_{mp}= 24.0 V
		I_{mp}= 7.71 A
		P_{mp}= 185 W
		3 protection diodes

The *HF Process* allows the detection of a healthy state or failure state. If healthy, the message *Hty State* appears on one display. Nevertheless, if a failure state is detected, then the next level of analysis is performed. The level is called *FS1 Process*. Therein, a specific type of condition present in the PVS is located. If this failure is detected, the message *FS1 State* is shown to the user. If this failure is not detected, then the *FS2 Process* is applied, identifying whether the *FS2* condition is present. If this failure is detected, the message *FS2 State* will appear on display. Otherwise, the message *FS3 State* will appear. The *FS1 Process* to *FS3 Process* do not refer to a specific condition of the PVS. In other words, the failure cases to be detected and their decision-making sequence are not defined but will be established based on the general behavior of the PVG to be evaluated.

IV. SIMULATION OF AN ELECTRICAL GRID CONNECTED PVG

The simulation of a grid-connected PVG was carried out to demonstrate the dependences between the PVS-PVI signal and the irradiance conditions. Table 1 shows the tests carried out in the simulation. The v_{str} and i_{str} signals were measured for each simulation.

The Photovoltaics library from OpenModelica was used as a computational tool. The simulated PVS contained three PVMs, and each PVM had three protection diodes. The model of the PVM used and its characteristics are shown in Table 2. The PVI is a single-phase type, and it was designed with an H bridge with semiconductor device technology. The electrical grid has a voltage of 110 V and a frequency of 60 Hz. The electrical diagram of the simulation is shown in Fig. 13.

V. EXPERIMENTAL CONFIGURATION AND CASE STUDIES

Experimental tests were carried out to evaluate the proposed method. Two PVGs of different characteristics were studied, which were called PVG1 and PVG2, and their PVSs were called PVS1 and PVS2. The tests demonstrate the efficiency of the proposed method because each of the used PVSs has a different response in ripple voltage. Also, the PVMs used at each site are from different manufacturers and with different

where *j* is the number of neighbors to consider in the evaluation. A graphical representation of the Euclidean distance is shown in Fig. 11, where elements *u*, *v*, and *w* surround the *Q* point. The distances, identified as d_u, d_v, and d_w, are considered closest to the *Q* point. This point belongs to *Cat1* category because d_v and d_w belong to the this category.

The methodology mentioned above to locate the nearest neighbors is repeated for the processes indicated in Fig. 12. It should be noted that each of these processes has a smaller number of elements than the preceding process. The aforementioned is because decision-making is carried out each time for more specific cases.
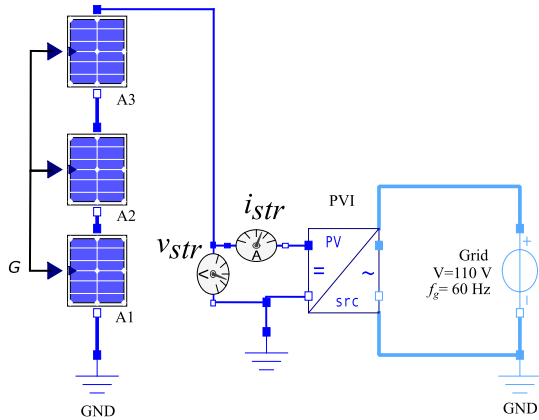
FIGURE 13. Electrical diagram of the grid-connected PVG used in the simulation.

TABLE 3. Test conditions.

Id	Description	Characteristics
Hty	State without failure	No PVM diode activated, no wire segment between ends of a PVM
$Ps1$	Partial shading	1 PVM diode activated
$Ps2$	Partial shading	2 PVM diode activated
$Ps3$	Partial shading	3 PVM diode activated
$Sc1$	Short circuit	Wire segment between PVM ends

internal configurations. The characteristics of each PVG will be described in case study 1 and case study 2 subsections.

The PVMs were identified as Aw with $w = 1, 2, \ldots, H$, where H is the maximum number of PVMs for each PVS. The experimental tests were carried out with the PVMs under different conditions. Table 3 shows these conditions, along with their identifiers and characteristics. It was verified that there were no interferences on the PVMs surface for the Hty condition.

The $Ps1$, $Ps2$, and $Ps3$ conditions were created artificially through a canvas of non-transparent material. The canvas was placed in the lower segment of the PVM to activate the number of diodes corresponding to the type of condition (see Table 3). Finally, the $Sc1$ condition was induced similarly to what was carried out in [6]. This technique consists of placing a cable segment between the two ends of the PVM, which allows the passage of current with a minimum voltage drop.

The T, G, v_{str}, and i_{str} signals were measured in each test. The signals were acquired at 8-second intervals and were stored sequentially in the $dbV[j_p]$ matrix. The experimental settings are shown in Fig. 14, and the PVS for each case is shown in Fig. 15. The T signal was measured with a model DS18B20 digital thermometer placed in direct contact with one of the PVMs. On the other hand, the G signal was measured with a Vaisala brand QMS101 pyranometer. This sensor is analog with a linear response and a sensitivity of 75 μ V/Wm^{-2}. The sensor was placed parallel to the plane of inclination of the PVS. Because the sensor is analog, an ADC1115 analog-to-digital converter (ADC) was used, with 16 conversion bits and 1Wire communication.
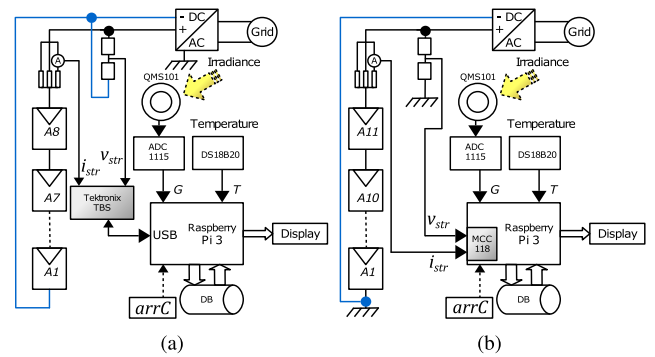

FIGURE 14. Experimental setup (a) Electrical diagram of PVG1, and (b) Electrical diagram of PVG2.

(a)

(b)

FIGURE 15. Photovoltaic strings used in: (a) PVG1, and (b) PVG2.

The v_{str} and i_{str} signals were conditioned before the measurement. A resistive voltage divider and a resistive current divider were used for this purpose. This conditioning was due to the voltage levels required by the system or data acquisition card (DAQ). A third of the i_{str} signal was measured after conditioning, via an ACS712 current sensor with an analog output.

1000 samples were processed in all the study cases. This number is half the number of acquired samples. This process allows more stable data to be processed by selecting a segment with the least difference between its minimum and maximum value.

Performance analysis of the KNN response was performed for the final choice of j. The training response was analyzed with 70%, 60%, and 50% of the recorded $dbV[j_p]$ vectors. Furthermore, the values of j from 1 to 15 were tested for each of these cases. The amount of input data for training depends on the records found in the $dbV[j_p]$ vector. Finally,

TABLE 4. Characteristics of materials and equipment used.

PVG	Id	Description	Characteristics
PVG1	DC–AC	Grid connected inverter ABB, model 5k	$P_{\max}$= 5 kW
	PVM	Photovoltaic module SAYA model SAYA-M150-28	28 solar cells V_{oc}= 18.74 V I_{sc}= 9.85 A V_{mp}= 15.6 V I_{mp}= 9.38 A P_{mp}= 150 W 2 protection diodes
	Grid	Utility grid	f_g= 60 Hz V_g= 110 V_{ac}
PVG2	DC–AC	Grid connected inverter Sunny Boy, model SB 5000US	$P_{\max}$= 5 kW
	PVM	Photovoltaic module Kyocera model KD240GX-LFB	60 solar cells V_{oc}= 36.9 V I_{sc}= 8.59A V_{mp}= 29.8 V I_{mp}= 8.06 A P_{mp}= 240 W 3 protection diodes
	Grid	Utility grid	f_g = 60 Hz V_g= 110 V_{ac}

the detected condition of the PVS is displayed on a liquid crystal display (LCD).

A. CASE STUDY 1

Table 4 shows the characteristics of the PVG1 elements, and Fig. 14(a) shows the block diagram of the experimental setup of this case study. The PVG1 has 8 PVMs, identified from $A1$ to $A8$ (see Fig. 15(a)). The negative terminal of the PVS1 is not connected to the ground of the $DC - AC$ converter. This configuration is due to the characteristics of the PVI. The resistive voltage divider was set to provide 5.4% of v_{str}. On the other hand, the i_{str} signal was measured through an ACS712-5 sensor, with a maximum measurement range of 5 A and a resolution of 180 mV/A. A TBS1102B-EDU Tektronix oscilloscope was used for data acquisition. The control of communication via USB and data processing were implemented on a Raspberry Pi 3 card, using the Python language. The v_{str} and i_{str} signals were acquired with a sampling frequency of 5 kS/s, and 2000 samples were acquired per period. On the other hand, Table 3 shows the test conditions of the PVMs. The $Ps3$ case was not carried out because the PVMs used only have two protection diodes.

The $dbV[j_p]$ matrix considered for the KNN network training were established within a range of temperatures and irradiances. The T signal range was from 26 °C to 34 °C, whereas G signal range was from 400 Wm^{-2} to 1000 Wm^{-2}.

B. CASE STUDY 2

Table 4 shows the characteristics of the PVG2 elements. The block diagram of the experimental configuration of this case study is shown in Fig. 14(b). The PVG2 has 11 PVMs, identified from $A1$ to $A11$ (see Fig. 15(b)). Furthermore,
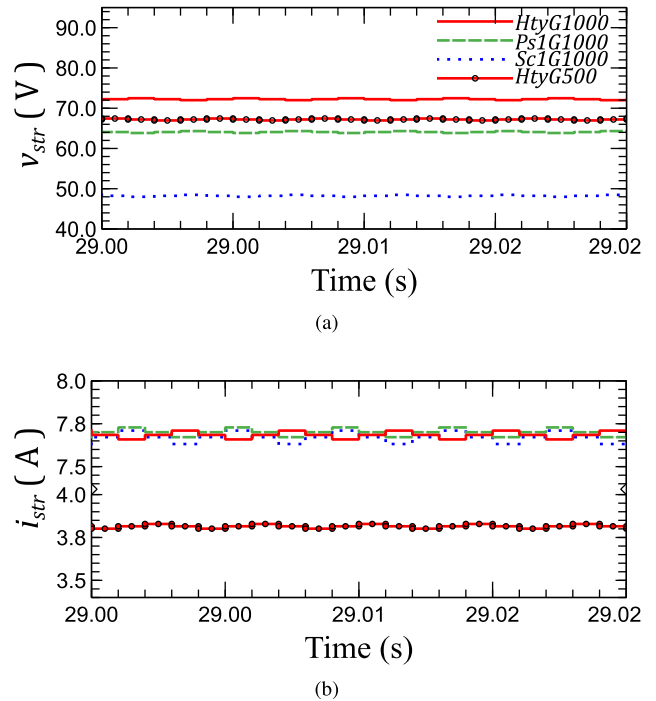

FIGURE 16. Results of the simulation of a PVG at different irradiance conditions. (a) Signal v_{str} in the time domain. (b) i_{str} signal in the time domain.

the negative terminal of the PVS2 is connected to the ground of the DC-AC converter, unlike PVG1. This connection is because this PVI has different features than those PVI used in case study 1. The resistive voltage divider was set to provide 2.54% of v_{str}. The i_{str} signal was measured through a sensor model ACS712-20, with a maximum measurement range of 20 A, and a resolution of 100 mV/A.

A 12-bit DAQ MCC118 Measurement Computing was used for data acquisition. DAQ control and data processing were implemented on a Raspberry Pi 3 card, using the Python language. The i_{str} and v_{str} signals were acquired with a sampling frequency of 2 kS/s, and 2000 samples were acquired during each period. Table 3 shows conditions analyzed.

The range of temperatures and irradiances considered for the $dbV[j_p]$ matrix were different from the temperatures and irradiances of the case study 1. The T signal and G signal ranges were from 40 °C to 50 °C and from 700 Wm^{-2} to 1000 Wm^{-2}.

VI. RESULTS

This section analyzes the results obtained from the simulation of a grid-connected PVG and the results obtained from the experimental tests when applying the failure detection method to two PVGs with different characteristics.

A. SIMULATION RESULTS OF A GRID-CONNECTED PVG

The results of the simulation of a grid-connected PVG are shown in Fig. 16(a). The figure shows that the DC displacement of the v_{str} signal and the low voltage component frequency amplitude are modified when the irradiance changes.

Furthermore, voltage changes due to partial shading and short circuit conditions are agree with Eqs. 5 and 6, respectively. Figure 16(b) shows that the i_{str} signal also experiences an adjustment in its waveform when the irradiance changes; these changes agree with Eq. 4.

B. EXPERIMENTAL RESULTS OF CASE STUDY 1

The results of the first case study are analyzed below. Figure 17(a) and (c) shows three segments of the v_{str} and i_{str} signals obtained from the experimental tests of the PVG1. The figure includes the results of all the conditions performed on the PVMs (Table 3). Figure 17 shows that the v_{str} and i_{str} signals have a DC shift. Also, a set of different frequencies can be noticed. These results agree with the simulation. Furthermore, Fig. 17(a) shows that the v_{str} signals have a low-frequency component, which causes overlap between the v_{str} signals obtained under different conditions. The aforementioned makes it difficult to immediately identify the condition to which a specific v_{str} signal belongs. Therefore, it is necessary to analyze the signal in the frequency domain.

Figure 17(c) shows that the i_{str} signals obtained in the PVG1 present small oscillations in the order of tenths of Ampere, which are not so significant. However, in some instants of time, there are current peaks with amplitudes bigger than 1 A. These current peaks affect the results of the analysis in the frequency domain. Therefore, measurements showing this type of oscillation should be discarded. Furthermore, Fig. 17(c) shows that for some PVS1 conditions, i_{str} signal levels are overlapping, which makes their detection difficult.

On the other hand, Fig. 18(a) shows a three-dimensional Cartesian plane containing the normalized magnitudes of the frequency components $V_F[a_0]$, $V_F[a_{2fg}]$, and $I_F[a_0]$. These components correspond to the frequencies of 0 Hz and 120 Hz of the signals v_{str} and i_{str}. The signals were obtained experimentally from the PVG1 under some conditions presented in Table 3. Figure 18 shows only a representative subset of the data experimentally obtained from PVG1. This subset belongs to tests with the T signal range from 30 °C to 31 °C, whereas the G signal range was from 400 Wm^{-2} to 1000 Wm^{-2}.

Figure 18(b) shows that the normalized magnitudes, belonging to the frequency components for the *Hty* and *Ps*1 conditions, are located in octant I. Figure 18(c) shows that the magnitudes belonging to the *Sc*1 condition are located in octant V. Finally, Fig. 18(d) shows that the normalized magnitudes of the frequency components for *Ps*2 and *Sc*1 conditions are located in octants V and VI, respectively. In general, Fig. 18 shows that each condition of the PVS1 is located mostly in different octants. Therefore, the state of the PVS1 can be identified from their vector of frequency components. The small dispersions that occur in some cases are solved by using the KNN technique. Table 5 shows the K_n vector values obtained during the KNN training of the PVG1.

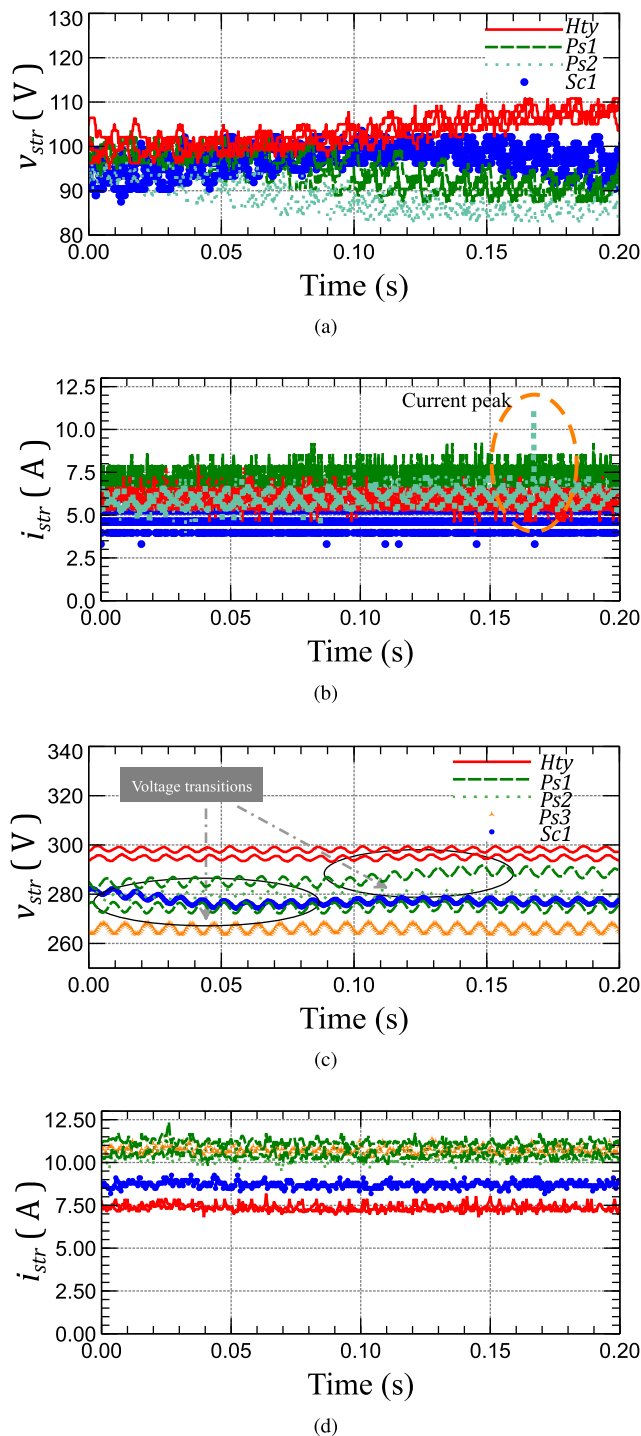Table 6 shows the exclusive sequence of evaluation proposed for the decision-making in the PVG1. The sequence is

(a)

(b)

(c)

(d)

FIGURE 17. Signals in the time domain obtained from the PVGs used in the experimentation. (a) v_{str} from PVG1, (b) i_{str} from PVG1, (c) v_{str} from PVG2, (d) i_{str} from PVG2.

based on the analysis of the distribution of normalized magnitudes of Figures 18 and 12. The last evaluated conditions are the coordinates of the *Ps*2 and *Sc*1 conditions. It is because they are very closed in the *Fs*2 process.

Figure 19(a) shows the results of the KNN efficiency of PVG1, obtained during its training. The figure shows that the best performances of the KNN are obtained with 70% and
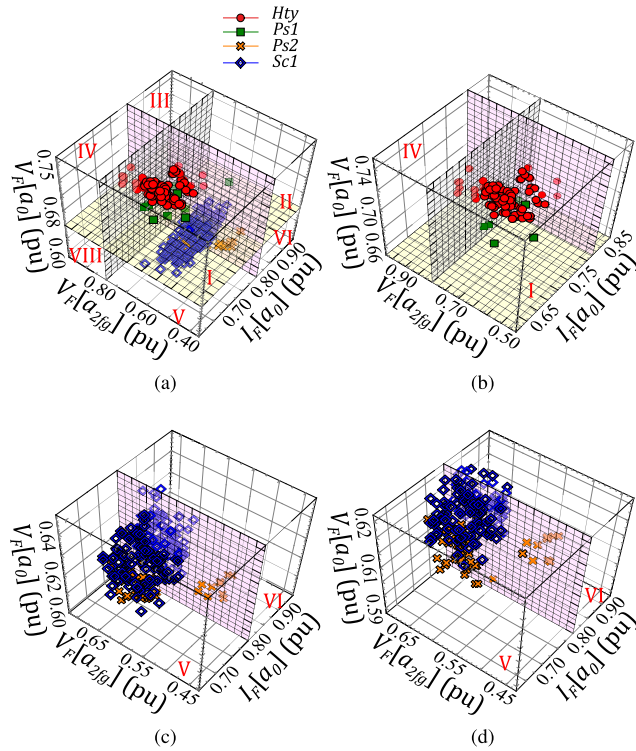
FIGURE 18. Set of normalized values for various conditions of the PVS1: (a) data universe, (b) regions for *Hty* and *Ps*1 conditions, (c) regions for *Ps*2 and *Sc*1 conditions, and (d) approach to the region for *Ps*2 condition.

TABLE 5. Values obtained of K_n for the PVG1 and PVG2.

PGV	K_1	K_2	K_3	K_4	K_5
1	25	1000	75565	10121	13868
2	25	100	$220E3$	900	$15E3$

TABLE 6. Proposed evaluation sequence for the case studies.

PVG	Process	Decision making	
		If true	*If false*
PVG1	*HF*	*Hty*	Some failure
	*FS*1	*Ps*1	*Ps*1 or *Sc*1
	*FS*2	*Ps*2	*Sc*1
PVG2	*HF*	*Hty*	Some failure
	*FS*1	*Sc*1	*Ps*1, *Ps*2, or *Ps*3
	*FS*2	*Ps*1	*Ps*2 or *Ps*3

60% of the recorded $dbV[j_p]$ matrix. It can also be observed that there is a coincidence between the three performances analyzed when j takes a value of 9. Therefore, the value of 9 was chosen as the number of nearest neighbors to be considered at all evaluation levels.

Figure 20 shows the results of the evaluation sequence (Table 6) for the decision-making. The results belong to the condition of the 741 test cases of the PVG1. The figure shows a 97% effectiveness in detecting Hty conditions and 100% effectiveness in detecting the presence of failures. Out of this 100%, it was 100% effective in detecting the *Ps*1 condition but was only 97% effective for detecting any *Ps*2 and *Sc*1
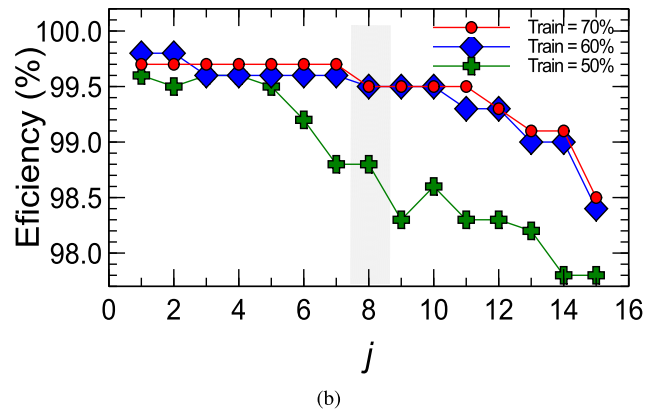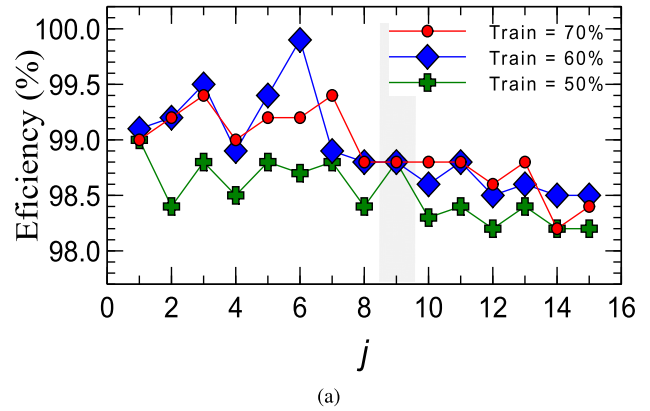

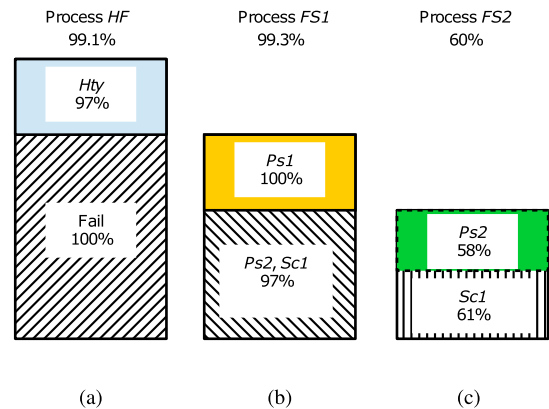**FIGURE 19.** KNN efficiency of the (a) PVG1, and (b) PVG2.

FIGURE 20. Effectiveness of condition detection in the PVG1. (a) HF Process, (b) FS1 Process, and (c) FS2 Process.

conditions. Finally, out of this 97%, a 58% effectiveness was obtained when detecting the *Ps*2 condition, and a 61% effectiveness for *Sc*1 condition.

C. EXPERIMENTAL RESULTS OF CASE STUDY 2
Figure 17(b) and (d) shows three segments of the v_{str} and i_{str} signals obtained from experimental tests of the PVG2. The figure includes the results of all the conditions presented in Table 3. The figure shows that the v_{str} and i_{str} signals show a DC shift, which coincides with the results obtained
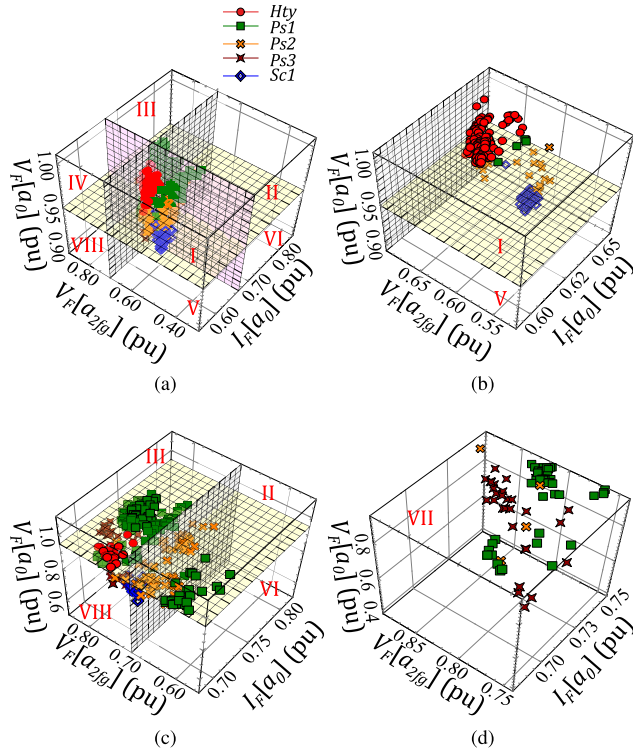
FIGURE 21. Set of normalized values for different conditions of the PVS2: (a) Universe of data, (b) Regions for *Hty* and *Sc*1 conditions, (c) Regions for the *Ps*1 and *Ps*2 conditions, and (d) Region for the *Ps*3 condition.

FIGURE 22. Effectiveness of detection in the condition of the PVG2. (a) *HF* Process, (b) *FS1* Process, and (c) *FS2* Process.

in the PVG1. Similarly, the set of different frequencies of the PVI2 operation can be noticed. Figure 17(b) shows that the v_{str} signal levels have a transition in some conditions of the PVS, whose slope can be positive or negative. This slope causes that, under different PVS conditions, the v_{str} signals overlap each other and make it difficult to immediately identify the condition to which a given v_{str} signal belongs. The amplitude of the low-frequency signal is not determined directly. Therefore, it is necessary to analyze this signal in the frequency domain.

On the other hand, Fig. 17(d) presents the i_{str} signals obtained in the PVG2. Although the i_{str} signals show lower oscillations than the i_{str} signals obtained from the PVG1, and although for the PVG2, there are no current peaks with amplitudes bigger than 1 A, as happened for the PVG1, it is not possible to detect some conditions of the PVS2. The i_{str} signals levels are overlapping for some conditions, as was the case for conditions of the PVS1.

Figure 21(a) shows a three-dimensional Cartesian plane containing the normalized magnitudes of the frequency components $V_F[a_0]$, $V_F[a_{2fg}]$, and $I_F[a_0]$. These components correspond to 0 Hz and 120 Hz frequencies of the v_{str} and i_{str} signals, which were obtained experimentally from the PVG2 under the conditions specified in Table 3. Only a representative subset of the experimental data obtained from the PVG2 is shown in Fig. 21. This subset belongs to the *T* signal tests in a range from 40 °C to 45 °C. As for the *G* signal, values range from 800 Wm^{-2} to 1000 Wm^{-2}.
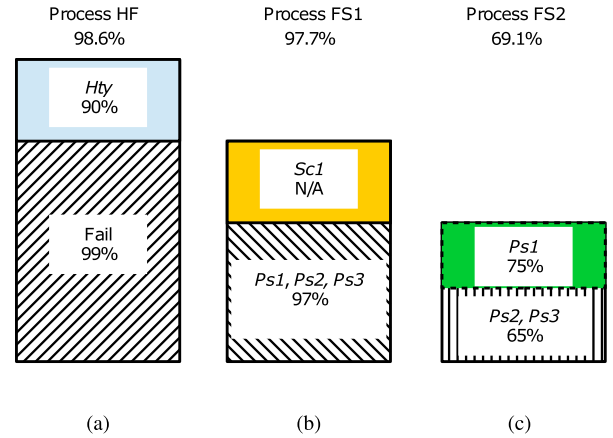
Figure 21(b) shows that the normalized magnitudes of the frequency components for the *Hty* condition are located in the octant I. In contrast, the magnitudes of the *Sc*1 condition are found in the octant V. Figure 21(c) shows that the normalized magnitudes of the frequency components for the *Ps*1 and *Ps*2 condition are located in the octant II and VI, respectively. Finally, Fig. 21(d) shows that the magnitudes for the *Ps*3 condition are located in octant VIII. In general, Fig. 21 shows that each PVS condition is located mostly in different octants. Therefore, the condition of the PVS2 can be identified from their vector of frequency components. The small dispersions that occur in some cases are solved by using the KNN algorithm. Table 5 shows the values of the K_n vector for the PVG2.

Table 6 shows the exclusive sequence of evaluation proposed for decision-making in the PVG2. The sequence was obtained from the analysis of the distribution of normalized magnitudes presented in Fig. 21. The *Ps*2 and *Ps*3 conditions are in the same category because they show similar results.

Figure 19(b) shows the results of the efficiency of the KNN of the PVG2, obtained during training. This figure shows that the best performances of the KNN are obtained with 70% and 60% of the recorded $dbV[j_p]$ matrix. The results are the same as the obtained from the PVG1. There is a coincidence between the two best performances when the number of nearest neighbors to be considered at all evaluation levels is 8.

Figure 22 shows the results of the evaluation sequence presented in Table 6. The results belong to the decision-making in all 650 test cases on the PVG2. The figure shows that the proposed methodology is 90% effective in detecting *Hty* conditions and 99% effective in indicating the presence of a failure. Out of this 99%, it was 97% effective in detecting conditions due to some level of partial shading. Furthermore, this third level of detection has a 75% effectiveness in detecting *Ps*1 condition and 65% effectiveness for detecting *Ps*2 or *Ps*3 conditions. Validation tests for the *Sc*1 condition were not carried out.

TABLE 7. Comparative between proposed methodology and methods described in [2], [5], and [12].

Feature	[2]	[5]	[12]	Proposed methodology
Variables	G, T, P	V_{oc}, V_{mp}, R_s	i_{str}	G, T, v_{str}, i_{str}
Simulation	✓	X	X	X
Technique	Analytical method	Multiple techniques	Statistical comparisons	KNN
PV System	15 W	3.1 kW, 3.9 kW	168 W	1.2 kW, 2.5 kW
Grid-tied	X	X	X	✓
I-V curve	X	✓	X	X
Training	✓	✓	X	✓
Parameter calculation	Diverse coefficients	Normalization	mean, median, quartiles	DFT, normalization
Special devices	MPPT, Electronic load	Sliding varistor, Solar system analyser	Two reference PVM, Current sensor by string	X
Architecture of PVM	X	X	X	✓
Number of faults	2	3	5	2

VII. DISCUSSIONS

The classic proposals for the monitoring of photovoltaic systems consider ideal performance conditions. However, in order to subject them to real performance conditions, adjustments to some parameters are necessary. Moreover, there are methodologies whose operation depends on the $I - V$ curve of the set of PVM used. The procedure to obtain the $I - V$ curve involves stopping energy production in a PVS or PVA. These are some of the features that limit applying this type of methodologies in real operating environments.

Table 7 provides a comparison between the proposed methodology and the methods described in [2], [5], and [12]. In [2], it is necessary to compare the theoretical power of each PVS against its generated power at a given instant. A measuring device is used per each PVS, making the application of the methodology costly. On other hand, the proposed method in [5] uses a PVM of the entire PVS as a reference. The selection of the PVM with least deviation is difficult to perform in large photovoltaic systems. In [12], the current generated by each PVS is compared against the others. This proposal only considers systems that have more than one string in parallel. None of the three aforementioned methods considers the architecture of PVMs; and in some cases, the PVMs used are not applicable in real environments.

Regarding the present proposal, two considerations must be taken into account before applying the described methodology. First, it is necessary to have a DB with all the cases to consider in the training stage. The lack of DB will cause a delay in the initial stage of the process. Regarding the second consideration, the DFT calculation can consume many resources. Therefore, it is recommended to perform an analysis to obtain the appropriate number of samples per sampling period.

VIII. CONCLUSION

In this work, a method for determining the condition of a grid-connected PVG is presented. The developed methodology allowed detecting if the PVMs of a PVG are in healthy conditions or failure conditions. The methodology detects anomalies and indicates if the failure is due to a PVM in a short circuit or the failure is due to partial shading. The method indicates the number of protection diodes that were

activated if the last condition arises. The proposed methodology does not require specialized sensors nor specific conditions that affect the electrical installation present in the PVS, unlike other techniques. These characteristics allow adapting the evaluation based on the general behavior of the PVG. The considered environmental variables are temperature and irradiance, whereas the electrical variables of interest are the voltage and current generated from the interaction between the PVS and the PVI.

The magnitudes of 0 Hz and $2f_g$ Hz components are used from the voltage signal, and only the magnitude of the 0 Hz component is used from the current signal. Cartesian coordinates are formed from these magnitudes and graphed in a three-dimensional space. The coordinates belonging to each of the PVS conditions are mostly located in different octants. This distribution allowed for the detection of the condition of the array based on its location. The small dispersions that occur in some cases are solved using the KNN technique, which allows differentiating between conditions that are very close to each other. The simplicity in implementing the techniques used makes it possible to use devices with low computational power, which is reflected in the decrease in costs. An additional advantage of the proposed technique is that it has a training stage, which allows it to adapt to the performance conditions of different PVGs.

The simulation of a grid-connected PVG was carried out as a first approximation to the analyzed phenomenon. The simulation showed that the voltage and current signals generated from the interaction between the PVS and the PVI are modified as a function of the conditions of the PVS.

On the other hand, the effectiveness of the proposed methodology was experimentally validated in two grid-connected PVGs, which have different characteristics. The detection results show effectiveness greater than 90% in the first evaluation levels, whereas there is a slightly lower detection certainty in anomalous conditions with coordinates that are very close to each other. However, the system has 100% certainty when detecting the presence of an abnormal condition.

Finally, the proposed methodology could be included as an additional element in the design of new PVIs, which offers PVGs users a tool to obtain a better performance or avoid

accidents. It is according to the results and characteristics of the signals used.

REFERENCES

[1] M. Schmela, "SolarPower Europe (2020): Global market outlook for solar power 2020–2024," Solar Power Eur., Rue d'Arlon 69-71, Brussels, Belgium, Tech. Rep., Jun. 2020.

[2] N. Gokmen, E. Karatepe, B. Celik, and S. Silvestre, "Simple diagnostic approach for determining of faulted PV modules in string based PV arrays," *Sol. Energy*, vol. 86, no. 11, pp. 3364–3377, Nov. 2012.

[3] A. Sabry, Z. M. Mohammed, F. H. Nordin, N. H. Nik Ali, and A. S. Al-Ogaili, "Single-phase grid-tied transformerless inverter of zero leakage current for PV system," *IEEE Access*, vol. 8, pp. 4361–4371, 2020.

[4] G. Liu, W. Yu, and L. Zhu, "Condition classification and performance of mismatched photovoltaic arrays via a pre-filtered elman neural network decision making tool," *Sol. Energy*, vol. 173, pp. 1011–1024, Oct. 2018.

[5] J.-M. Huang, R.-J. Wai, and W. Gao, "Newly-designed fault diagnostic method for solar photovoltaic generation system based on IV-curve measurement," *IEEE Access*, vol. 7, pp. 70919–70932, 2019.

[6] Z. Chen, L. Wu, S. Cheng, P. Lin, Y. Wu, and W. Lin, "Intelligent fault diagnosis of photovoltaic arrays based on optimized kernel extreme learning machine and I-V characteristics," *Appl. Energy*, vol. 204, pp. 912–931, Oct. 2017.

[7] M. Davarifar, A. Rabhi, A. Hajjaji, E. Kamal, and Z. Daneshifar, "Partial shading fault diagnosis in PV system with discrete wavelet transform (dwt)," in *Proc. 3rd Int. Conf. Renew. Energy Res. Appl. ICRERA*, Oct. 2014, pp. 810–814.

[8] P. Satpathy, R. Sharma, and S. Dash, "An efficient sd-par technique for maximum power generation from modules of partially shaded pv arrays," *Energy*, vol. 175, pp. 182–194, 2019.

[9] C. B. Jones, M. Martinez-Ramon, R. Smith, C. K. Carmignani, O. Lavrova, C. Robinson, and J. S. Stein, "Automatic fault classification of photovoltaic strings based on an *in situ* IV characterization system and a Gaussian process algorithm," in *Proc. IEEE 43rd Photovoltaic Spec. Conf. (PVSC)*, Jun. 2016, pp. 1–6.

[10] S. R. Madeti and S. N. Singh, "Modeling of PV system based on experimental data for fault detection using kNN method," *Sol. Energy*, vol. 173, pp. 139–151, Oct. 2018.

[11] T. Takashima, J. Yamaguchi, K. Otani, T. Oozeki, K. Kato, and M. Ishida, "Experimental studies of fault location in PV module strings," *Sol. Energy Mater. Sol. Cells*, vol. 93, nos. 6–7, pp. 1079–1082, Jun. 2009.

[12] Y. Zhao, B. Lehman, R. Ball, J. Mosesian, and J.-F. de Palma, "Outlier detection rules for fault detection in solar photovoltaic arrays," in *Proc. 28th Annu. IEEE Appl. Power Electron. Conf. Expo. (APEC)*, Mar. 2013, pp. 2913–2920.

[13] P.-Y. Sevilla-Camacho, M.-A. Zuniga-Reyes, J.-B. Robles-Ocampo, R. Castillo-Palomera, J. Muniz, and J. Rodriguez-Resendiz, "A novel fault detection and location method for PV arrays based on frequency analysis," *IEEE Access*, vol. 7, pp. 72050–72061, 2019.

[14] Y. Hu, W. Cao, S. Member, J. Ma, S. Finney, and D. Li, "Identifiying pv module mismatch faults by a thermography-based temperature distribution analysis," *IEEE Trans. Device Mater. Reliab*, vol. 18, no. 4, pp. 951–960, Dec. 2019.

[15] D. S. Pillai and N. Rajasekar, "An MPPT-based sensorless line–line and line–ground fault detection technique for PV systems," *IEEE Trans. Power Electron.*, vol. 34, no. 9, pp. 8646–8659, Sep. 2019.

[16] G. Ertasgin, D. Whaley, N. Ertugrul, and W. Soong, "Analysis of dc link energy storage for single-phase grid-connected pv inverters," *Electron*, vol. 8, no. 6, pp. 1–19, 2019.

[17] C. Meza and R. Ortega, "Control and estimation scheme for PV central inverters," in *Proc. 24th Int. Conf. Inf., Commun. Autom. Technol. (ICAT)*, Oct. 2013, pp. 1–6.

[18] D. Casadei, G. Grandi, and C. Rossi, "Single-phase single-stage photovoltaic generation system based on a ripple correlation control maximum power point tracking," *IEEE Trans. Energy Convers.*, vol. 21, no. 2, pp. 562–568, Jun. 2006.

[19] H. Lopez, J. R. Resendiz, X. Guo, N. Vazquez, and R. V. Carrillo-Serrano, "Transformerless common-mode current-source inverter grid-connected for PV applications," *IEEE Access*, vol. 6, pp. 62944–62953, 2018.

[20] S. B. Kjaer, J. K. Pedersen, and F. Blaabjerg, "A review of single-phase grid-connected inverters for photovoltaic modules," *IEEE Trans. Ind. Appl.*, vol. 41, no. 5, pp. 1292–1306, Sep. 2005.

[21] A. H. El Khateb, N. A. Rahim, J. Selvaraj, and B. W. Williams, "DC-to-DC converter with low input current ripple for maximum photovoltaic power extraction," *IEEE Trans. Ind. Electron.*, vol. 62, no. 4, pp. 2246–2256, Apr. 2015.

[22] M. Vujacic, M. Hammami, M. Srndovic, and G. Grandi, "Analysis of DC-link voltage switching ripple in three-phase PWM inverters," *Energies*, vol. 11, no. 2, p. 471, Feb. 2018.

[23] R. Kaplar, R. Brock, S. DasGupta, M. Marinella, A. Starbuck, A. Fresquez, S. Gonzalez, J. Granata, M. Quintana, M. Smith, and S. Atcitty, "PV inverter performance and reliability: What is the role of the IGBT?" in *Proc. 37th IEEE Photovoltaic Spec. Conf.*, Jun. 2011, Art. no. 001842.

[24] M. Barghi Latran and A. Teke, "Investigation of multilevel multifunctional grid connected inverter topologies and control strategies used in photovoltaic systems," *Renew. Sustain. Energy Rev.*, vol. 42, pp. 361–376, Feb. 2015.

[25] H. Chaieb and A. Sakly, "A novel MPPT method for photovoltaic application under partial shaded conditions," *Sol. Energy*, vol. 159, pp. 291–299, Jan. 2018.

[26] D. S. Pillai, F. Blaabjerg, and N. Rajasekar, "A comparative evaluation of advanced fault detection approaches for PV systems," *IEEE J. Photovolt.*, vol. 9, no. 2, pp. 513–527, Mar. 2019.

[27] J. Hosseinzadeh, F. Masoodzadeh, and E. Roshandel, "Fault detection and classification in smart grids using augmented K-NN algorithm," *Social Netw. Appl. Sci.*, vol. 1, no. 12, pp. 1–13, Dec. 2019.

MARCO-ANTONIO ZUÑIGA-REYES (Member, IEEE) received the B.S. degree in electronics engineering from the Instituto Tecnológico de Tuxtla Gutiérrez (ITTG), México, in 1997, and the master's degree in renewable energy from the Universidad Politécnica de Chiapas (UPChiapas), in 2016. He is currently pursuing the Ph.D. degree with the Universidad de Ciencias y Artes de Chiapas (UNICACH), Mexico.

JOSE-BILLERMAN ROBLES-OCAMPO received the B.S. and master's degrees in mechanical engineering and the Ph.D. degree in engineering, in 2003, 2007, and 2012, respectively. He has been a Professor/a Researcher with the Universidad Politécnica de Chiapas (UPChiapas), since 2012. He has worked in renewable energy, fault detection in dynamics systems, and CNC machines. He is a member of the National System of Researchers (SNI), Mexico.

PERLA-YAZMÍN SEVILLA-CAMACHO received the B.S. and master's degree in electronics engineering from the Instituto Tecnológico de Celaya (ITTC), Guanajuato, Mexico, and the Ph.D. degree in engineering from the Universidad Autónoma de Queretaro (UAQ), Queretaro, Mexico, in 2012. Since 2007, she has been a Professor with the University Politécnica of Chiapas (UPChiapas). She is a member of the National System of Researchers (SNI), Mexico. Her current research interests include experimental and theoretical investigation of fault detection and condition monitoring applied to mechanical systems and renewable energy systems.

JUVENAL RODRÍGUEZ-RESÉNDIZ (Senior Member, IEEE) was as a Visiting Professor with West Virginia University, in 2012. He is currently the Co-ordinator of the Master of Automation with Querétaro State University (UAQ), México. He is also the Director of the Office for Partnership with Industry and Academy at UAQ. He teaches digital signal processing and research methodology courses at UAQ. He belongs to the Mexican Academy of Sciences, the Mexican Association of Robotics, the National Research Academy (SNI), Mexico. He has developed more than 40-industrial projects by linking UAQ and government. His team has published more than 80 technical and education articles. He patented more than ten innovations. He has been the Advisor of more than 200 theses of undergraduate, master, and doctoral grades. He has been invited to give 30 conferences around the world. He has won several national and international prizes because of his academic and innovation developments.

JORGE-EVARISTO CONDE-DÍAZ (Member, IEEE) received the B.S. degree in communications and electronics engineering from the National Technological of Mexico, Tuxtla Gutiérrez, Mexico, and the M.Sc. and Ph.D. degrees from the Solid-State Electronics Department, CINVESTAV, Mexico City, in 2005 and 2010, respectively. In 2007, he was on a research stay with the University Center FEI, Sao Bernardo do Campo, Brazil. He was a Research Scientist with The University of Texas at Dallas, from 2011 to 2012. He is currently working with Cátedras-CONACYT, Universidad de Ciencias y Artes de Chiapas, and the Counselor of the IEEE UNICACH Branch. He is a member of the National System of Researchers (SNI), Mexico.

• • •

ORLANDO LASTRES-DANGUILLECOURT received the B.S. degree in telecommunications engineering from the Julio Antonio Mella Higher Polytechnic Institute (ISPJAM), Santiago de Cuba, Cuba, in 1991, and the D.Sc. degree in engineering from the Energy Research Center (CIE), National Autonomous University of Mexico (UNAM), Mexico, in 2007. He was a Technologist of Research Development, from 1992 to 1993, a Researcher, from 1992 to 1993, and the Head of the Department of Wind Energy, from 1993 to 1995. From 1995 to 2002, he was the Director of the Solar Energy Research Center (CIES), Cuba. He has also worked as a Titular A Researcher Professor, from 2007 to 2010, as the Director of the Institute of Energy Studies, from 2008 to 2009, as the Chief of the Postgraduate Unit, from 2009 to 2010, as a Titular B Researcher Professor with ISTMO University (UNISTMO), from 2011 to 2016. He has been working as a Titular C Researcher Professor with the University of Sciences and Arts of Chiapas (UNICACH), since 2016. He is a member of the National System of Researchers (SNI), Mexico.